

# Bifocal Dual Reflectarray with Curved Main Surface

Antonio Pino <sup>1,\*</sup> , Yolanda Rodriguez-Vaqueiro <sup>1</sup>, Eduardo Martinez-de-Rioja <sup>2</sup> , Daniel Martinez-de-Rioja <sup>3</sup> , Borja González-Valdés <sup>1</sup>, Marcos Arias <sup>1</sup> , Oscar Rubiños <sup>1</sup> , José Antonio Encinar <sup>3</sup>  and Giovanni Toso <sup>4</sup> 

<sup>1</sup> AtlantTic Research Center for Telecommunication Technologies, Universidade de Vigo, 36310 Vigo, Spain; yrvaqueiro@com.uvigo.es (Y.R.-V.); bgvaldes@com.uvigo.es (B.G.-V.); marcos@com.uvigo.es (M.A.); oscar@com.uvigo.es (O.R.)

<sup>2</sup> Department of Signal Theory and Communications and Telematic Systems and Computing, Universidad Rey Juan Carlos, 28942 Fuenlabrada, Spain; eduardo.martinez@urjc.es

<sup>3</sup> Information Processing and Telecommunications Center, Universidad Politécnica de Madrid, 28040 Madrid, Spain; jd.martinezderioja@upm.es (D.M.-d.-R.); jose.encinar@upm.es (J.A.E.)

<sup>4</sup> European Space Research and Technology Centre (ESTEC), European Space Agency (ESA), 2201 AZ Noordwijk, The Netherlands; giovanni.toso@esa.int

\* Correspondence: agpino@com.uvigo.es; Tel.: +34-647343202

**Abstract:** This paper presents a novel approach to synthesizing curved reflectarrays using Geometrical Optics (GO). It introduces the concepts of virtual normal and path length shift, which enable a vector-based formulation of the problem that can be solved using ray tracing techniques. The formulation is applied for the design of two different versions of a Dual Bifocal Reflectarray with a parabolic main surface and a flat subreflectarray. The first version aims to enhance the performance of the multibeam antenna by providing a focal ring located at the feed cluster plane. The second version focuses on improving the scanning characteristics of the antenna in the horizontal plane by incorporating two foci. The synthesis procedure yields samples of the path length shift or its derivatives. To reconstruct the phase distribution, an interpolation scheme is employed and described in this paper. Numerical results are presented for both the focal-ring and two-foci configurations, demonstrating the feasibility of this solution for multibeam or scanning satellite antennas operating in the Ka.

**Keywords:** reflectarrays; bifocal; path length shift; virtual normal; multibeam antennas; scanning



**Citation:** Pino, A.; Rodriguez-Vaqueiro, Y.; Martinez-de-Rioja, E.; Martinez-de-Rioja, D.; González-Valdés, B.; Arias, M.; Rubiños, O.; Encinar, J.A.; Toso, G. Bifocal Dual Reflectarray with Curved Main Surface. *Electronics* **2023**, *12*, 2619. <https://doi.org/10.3390/electronics12122619>

Academic Editor: Dimitra I. Kaklamani

Received: 15 May 2023  
Revised: 4 June 2023  
Accepted: 8 June 2023  
Published: 10 June 2023



**Copyright:** © 2023 by the authors. Licensee MDPI, Basel, Switzerland. This article is an open access article distributed under the terms and conditions of the Creative Commons Attribution (CC BY) license (<https://creativecommons.org/licenses/by/4.0/>).

## 1. Introduction

Multibeam antennas for emerging communications satellites require an increasing number of spot beams that exploit different polarizations and frequencies [1]. The gain and beamwidth requirements of individual spots make it necessary to use of reflector or reflectarray systems fed by an appropriate cluster of feeding elements providing a color map of beams defined to achieve global coverage through frequency and polarization reuse. In a single-feed-per-beam (SFPB) configuration, due to the closely spaced beams required and the size limitation of the usable focal plane, traditional reflector antennas can provide only one color, and typically four reflector antennas are required, each operating in transmission (Tx) and reception (Rx). The field of view of these antennas, which is related to the scanning performance of the reflector or reflectarray systems, is one of the most critical factors in the design, due to the extensive use of the focal plane and the large coverage area compared to the size of a single beam.

It is known that bifocal dual reflector antennas [2–4] can improve the field of view of scanning antennas compared to the corresponding dual reflector versions with a single focus. The use of a dual reflector system introduces an additional degree of freedom, which can be utilized to ensure two privileged directions in the far field (or two focal targets in imaging applications) instead of requiring the condition that the main reflector and subreflector share a common focal point.

Reflectarray configurations have shown promise as solutions for multibeam antennas due to their ability to generate multiple beams using a single feed by polarization/frequency discrimination [5], or acting as a polarizer providing dual circular polarizations when illuminated by a signal in dual linear polarization [6].

The bifocal technique has been applied in dual reflectarray configurations [7–9] based on flat surfaces. In [7], a small size centered dual reflectarray antenna was proposed to improve the field of view in automotive radars operating in linear polarization. In [8], a procedure to compute the phase distribution of a bifocal dual reflectarray is presented for centered and offset configurations. In [9], a new bifocal design procedure for dual reflectarray antennas in offset configurations is presented. This procedure involves initially considering an axially symmetric geometry with the reflectarrays placed in parallel planes, and then tilting the reflectarray planes while readjusting the phases to avoid blockage effects.

For large aperture antennas, required for high gain multibeam antennas, using flat surface reflectarrays has the drawback of requiring a large phase adjustment with a high number of  $2\pi$  cycles. This adjustment is necessary to transform the spherical waves provided by the feeds into a large aperture with an almost uniform phase, which is crucial for providing narrow beams in high frequency bands such as the Ka-band commonly used for satellite communications. A promising technique is to combine the focusing advantages of curved reflector surfaces such as the paraboloid with the control of reflection properties available with reflectarray solutions. An example of this combination was proposed in [6] to design a polarizing reflector that transforms linear polarization into dual polarization.

The shaping techniques based on Geometrical Optics (GO), typically used for reflector antennas, such as the bifocal technique, can be generalized to reflectarray surfaces by using the modified Snell Law, when phase control is added to the surface. This paper presents a novel formulation that considers GO shaping techniques in curved reflectarrays. It is based on the concept of path length shift, which is proportional to the phase adjustment in reflectarray surfaces, and the concept of virtual normal, which allows for a vector formulation for GO shaping and analysis of curved reflectarrays. The technique is illustrated through the design of a bifocal dual reflectarray with flat subreflector and parabolic main reflectarray.

Section 2 and Appendix A present the treatment of the reflection equations for curved reflectarrays introducing the concepts of path length shift (proportional to the phase distribution) and the virtual normal (representing the reflection law at the reflectarray surface). Section 3 and Appendix B summarize the main characteristics of reflectarray analysis and synthesis for curved reflectarrays, as well as some interpolation algorithms for the treatment of the synthesized path length shift distributions that characterize the reflectarrays.

Section 4 presents the vector formulation of the bifocal synthesis algorithm applied to a curved reflectarray as the main surface fed from a flat sub-reflector. The synthesis of a line of data points is first formulated, followed by two examples of the 3D extension. Section 5 presents preliminary simulations of two different examples of bifocal reflectarrays defined for a multibeam satellite antenna in the Ka band. Finally, Section 6 presents the conclusions.

## 2. Reflection Equations for Curved Reflectarrays

Figure 1 represents a reflectarray surface described in Cartesian coordinates by the function  $z(x, y)$ . The partial derivatives of the function with respect  $x$  and  $y$  are denoted as  $z_x(x, y)$ ,  $z_y(x, y)$ , respectively. All of them are known “a priori”, as well as the unit normal vector to the surface, denoted as  $\hat{n}$ , which can be expressed as:

$$\hat{n} = \frac{-z_x\hat{x} - z_y\hat{y} + \hat{z}}{\sqrt{1 + z_x^2 + z_y^2}}. \quad (1)$$

The figure also depicts a generic reflection point  $R$ , along with the incident ray ( $\hat{i}$ ) and reflected ray ( $\hat{r}$ ). Figure 2 provides a detailed view of the reflection point and a local

reference system composed of the orthonormal vectors  $\{\hat{\alpha}, \hat{\beta}, \hat{n}\}$ , where  $\hat{\alpha}$  and  $\hat{\beta}$  lie in the tangent plane to the surface at  $R$ .

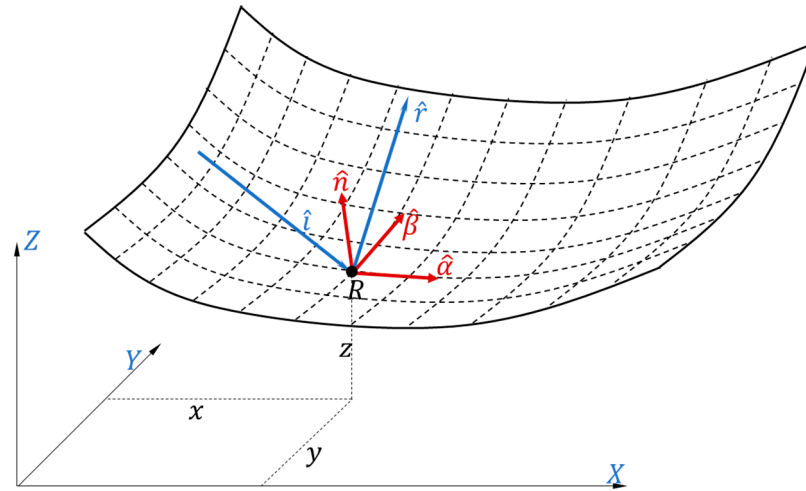


Figure 1. Absolute system and local system for the reflectarray surface.

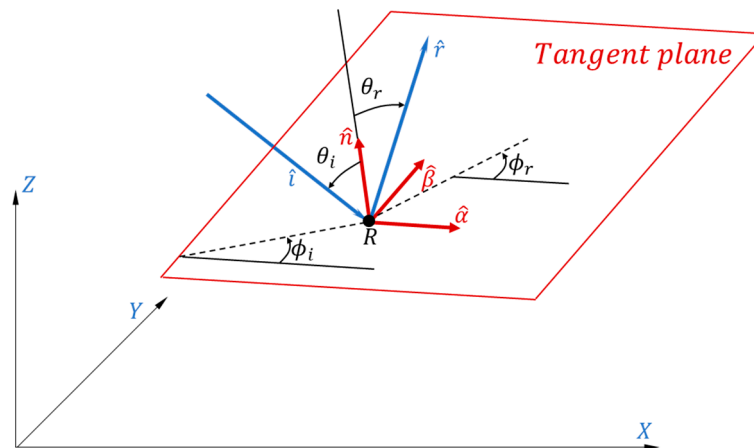


Figure 2. Detail of incident and reflection angles, and ray vectors.

For a reflectarray surface, a phase distribution denoted by  $\Phi(x, y)$  can be defined at each point of the surface, representing the phase control introduced by the local reflectarray elements. Let  $L(x, y)$  be the so-called path length shift, which is proportional to the phase shift introduced by the reflectarray elements at any point of the surface:

$$\Phi(x, y) = -kL(x, y) = -\frac{2\pi}{\lambda}L(x, y), \tag{2}$$

where  $k$  is the propagation constant.

The unit vectors corresponding to the incident and reflected rays can be expressed in the system shown in Figure 2 as:

$$\begin{aligned} \hat{r} &= \sin\theta_r \cos\phi_r \hat{\alpha} + \sin\theta_r \sin\phi_r \hat{\beta} + \cos\theta_r \hat{n}, \\ \hat{i} &= \sin\theta_i \cos\phi_i \hat{\alpha} + \sin\theta_i \sin\phi_i \hat{\beta} - \cos\theta_i \hat{n}. \end{aligned} \tag{3}$$

According to [10], the tangential components of  $\hat{i}$  and  $\hat{r}$  are related to the partial derivatives of the phase shift across the surface:

$$\begin{aligned} \sin\theta_r \cos\phi_r + \sin\theta_i \cos\phi_i &= -\frac{1}{k} \frac{\partial\Phi}{\partial\alpha} = \frac{\partial L}{\partial\alpha}, \\ \sin\theta_r \sin\phi_r + \sin\theta_i \sin\phi_i &= -\frac{1}{k} \frac{\partial\Phi}{\partial\beta} = \frac{\partial L}{\partial\beta}. \end{aligned} \tag{4}$$

The virtual normal is then defined at  $R$  as:

$$\vec{N} = \hat{r} - \hat{i}. \tag{5}$$

The main property of the virtual normal is that its tangential component  $\vec{N}_\tau$  is not dependent on the incidence angle of the ray  $\hat{i}$ , but it is directly related to the partial derivatives of  $\Phi$  along the two tangential variables  $\alpha, \beta$ , locally defined for the reflectarray surface around the reflection point  $R$ . The tangential vector  $\vec{N}_\tau$  can be represented both in the Cartesian system and in the local tangential system composed of  $\hat{\alpha}$  and  $\hat{\beta}$ :

$$\begin{aligned} \vec{N}_\tau &= N_x \hat{x} + N_y \hat{y} + N_z \hat{z} = N_\alpha \hat{\alpha} + N_\beta \hat{\beta}, \\ N_\alpha &= \frac{\partial L}{\partial\alpha}, N_\beta = \frac{\partial L}{\partial\beta}. \end{aligned} \tag{6}$$

Ray tracing techniques, which can be used to analyze a reflectarray, usually represent the rays in the absolute system  $\{\hat{x}, \hat{y}, \hat{z}\}$ . For planar reflectarrays, it is possible to define a local orthonormal system  $\{\hat{\alpha}, \hat{\beta}, \hat{n}\}$  at the center of the reflectarray, and the transformation between local coordinates and absolute coordinates in the system  $\{\hat{x}, \hat{y}, \hat{z}\}$  is simple and allows for connecting ray tracing in the absolute system to the reflectarray characterization through the path length shift distribution  $L(\alpha, \beta)$  in the local system  $\{\hat{\alpha}, \hat{\beta}, \hat{n}\}$ .

However, for curved reflectarrays, since the local system  $\{\hat{\alpha}, \hat{\beta}, \hat{n}\}$  varies across the surface, it is preferable to characterize the path length shift in the aperture domain through the function  $L(x, y)$ , where  $XY$  represents the aperture plane. As a result, it is necessary to relate the partial derivatives in the absolute system to the Cartesian components of  $\vec{N}_\tau$ . After some mathematical manipulations based on differential geometry (justified in detail in Appendix A), the following relation can be derived:

$$\begin{bmatrix} \frac{\partial L}{\partial x} \\ \frac{\partial L}{\partial y} \end{bmatrix} = \begin{bmatrix} 1 & 0 & z_x \\ 0 & 1 & z_y \end{bmatrix} \begin{bmatrix} N_x \\ N_y \\ N_z \end{bmatrix}. \tag{7}$$

For the synthesis problem of the reflectarray, it is necessary to express  $L(x, y)$  after determining  $\vec{N}_\tau$  using ray tracing techniques. This can be achieved by obtaining the partial derivatives using (7) and then integrating the derivatives or employing an interpolation scheme, as described in Appendix B.

For the analysis problem of the synthesized reflectarray by means of ray tracing techniques, the inverse relation required to order to evaluate the Cartesian components of  $\vec{N}_\tau$  in terms of the derivatives of  $L$  with respect to the aperture coordinates  $(x, y)$ . The following relation can also be derived by inverting (7), as described in Appendix A.

$$\begin{bmatrix} N_x \\ N_y \\ N_z \end{bmatrix} = \frac{1}{1 + z_x^2 + z_y^2} \begin{bmatrix} 1 + z_y^2 & -z_x z_y \\ -z_x z_y & 1 + z_x^2 \\ z_x & z_y \end{bmatrix} \begin{bmatrix} \frac{\partial L}{\partial x} \\ \frac{\partial L}{\partial y} \end{bmatrix}. \tag{8}$$

### 3. Geometrical Optics Analysis and Synthesis of Curved Reflectarrays

#### 3.1. Analysis Problem: Ray Tracing Algorithm to Obtain the Reflected or Incident Ray

The ray tracing technique can be utilized to calculate a reflected ray at the reflectarray surface when the incident ray is known and the function  $L(x, y)$  is characterized, as well as

its partial derivatives  $\partial L/\partial x$  and  $\partial L/\partial y$ . First, the intersection point  $R$  between the incident ray  $\hat{i}$  and the reflectarray surface  $z(x, y)$  is computed using geometric considerations, as well of the corresponding unit normal vector  $\hat{n}$ . Once the  $(x, y)$  coordinates of the reflection point are known, (8) allows us to obtain the tangential part  $\vec{N}_\tau$  of the virtual normal. The tangential part of the vector  $\hat{r}$  can be calculated by inverting (5), considering only the tangential components. Then, the reflected direction  $\hat{r}$  can be reconstructed by adding the normal component, ensuring that it remains a unit vector:

$$\vec{i}_\tau = \hat{i} - (\hat{i} \cdot \hat{n})\hat{n}, \quad \vec{r}_\tau = \vec{i}_\tau + \vec{N}_\tau, \quad \hat{r} = \vec{r}_\tau + \hat{n}\sqrt{1 - |\vec{r}_\tau|^2}. \tag{9}$$

If the incident vector must be determined from the reflected one, a similar procedure can be used, but considering the following equations:

$$\vec{r}_\tau = \hat{r} - (\hat{r} \cdot \hat{n})\hat{n}, \quad \vec{i}_\tau = \vec{r}_\tau - \vec{N}_\tau, \quad \hat{i} = \vec{i}_\tau - \hat{n}\sqrt{1 - |\vec{i}_\tau|^2}. \tag{10}$$

where the subindex  $\tau$  denotes the tangential part of the vectors.

### 3.2. Synthesis Problem: Ray Tracing Algorithms to Obtain the Path Length Shift Distribution across the Reflectarray

In the synthesis problem, the ray tracing technique is utilized to define the incident ( $\vec{i}_k$ ) and reflected ( $\vec{r}_k$ ) rays at a set of reflectarray points  $\{x_k, y_k, z_k\}$ , where  $z_k = z(x_k, y_k)$ . Additionally, the unit normal vector  $\hat{n}_k$  at each point is known. Since incident and reflected rays have been already described, the virtual normal  $\vec{N}_k$  at each point can be obtained using (5). The next step is to calculate the tangential component of each  $\vec{N}_k$  by subtracting the normal component:

$$\vec{N}_k = \vec{r}_k - \vec{i}_k \quad \vec{N}_{\tau k} = \vec{N}_k - (\vec{N}_k \cdot \hat{n}_k)\hat{n}_k. \tag{11}$$

Then, (6) can be used to compute the partial derivatives of  $L(x, y)$  at the set of data points across the reflectarray.

Alternatively, instead of using the reflection law, an eikonal condition can be applied, which assumes equal paths for the sum of the ray lengths along each trajectory. Let  $L_{Ek}$  denote the electrical length of ray  $k$ , and  $L_{Gk}$  its geometric length. The sum of the geometric length and the path length shift across the reflectarray represents the electrical length. In a synthesis problem, the electrical length is imposed by the designer, the geometric length is obtained from the ray tracing synthesis algorithm, and the path length shift across the reflectarray is unknown. Therefore, the following equation is used to describe the reflectarray path length shift:

$$L_k = L_{Ek} - L_{Gk}. \tag{12}$$

Once the path lengths shift  $\{L_k\}$ , its partial derivatives with respect to  $x$  and  $y$   $\{L_{xk}, L_{yk}\}$  or both are obtained for a set of data points, and an interpolation algorithm is required. A least squares scheme with polynomial basis functions is proposed to interpolate the synthesized data, allowing for a complete description of the path length function  $L(x, y)$ . This description enables the determination of the required phase shift for each element of the reflectarray based on the coordinates of the cell element. Two versions of this approximation are detailed in Appendix B, depending on the available data:  $L(x, y)$  or its partial derivatives.

### 4. Bifocal Dual Reflectarray with Parabolic Main Surface and Flat Subreflector Surface

#### 4.1. Synthesis Algorithm of a Linear Section

The proposed bifocal dual reflectarray consists of a parabolic main reflectarray surface, denoted as main-RA, and a flat subreflector reflectarray, denoted as sub-RA. This design aims to significantly reduce the phase adjustment requirements for the main reflectarray compared to using a flat reflectarray, as in [7–9].

The bifocal synthesis involves considering two reflectarray surfaces, main-RA and sub-RA, with two focal points ( $F_1, F_2$ ) and two focused scanned directions ( $\hat{s}_1, \hat{s}_2$ ). An algorithm is developed to obtain two lines of data points, which correspond to the main-RA and sub-RA, along with the virtual normal at each point. Figure 3 illustrates the bifocal synthesis for a 2D case. To start the synthesis process, a starting point is chosen at the main-RA, denoted as  $M_0$ , corresponding with unit normal vector  $\hat{n}_{M_0}$  and virtual normal vector  $\vec{N}_{M_0}$  obtained from (5) if the incident and reflected rays at the starting point  $M_0$  are known. Note that  $\vec{N}_{M_0}$  and  $\hat{n}_{M_0}$  are generally not collinear for reflectarray surfaces. In contrast, they would be collinear for a solid reflector surface without the ability to introduce phase shifts.

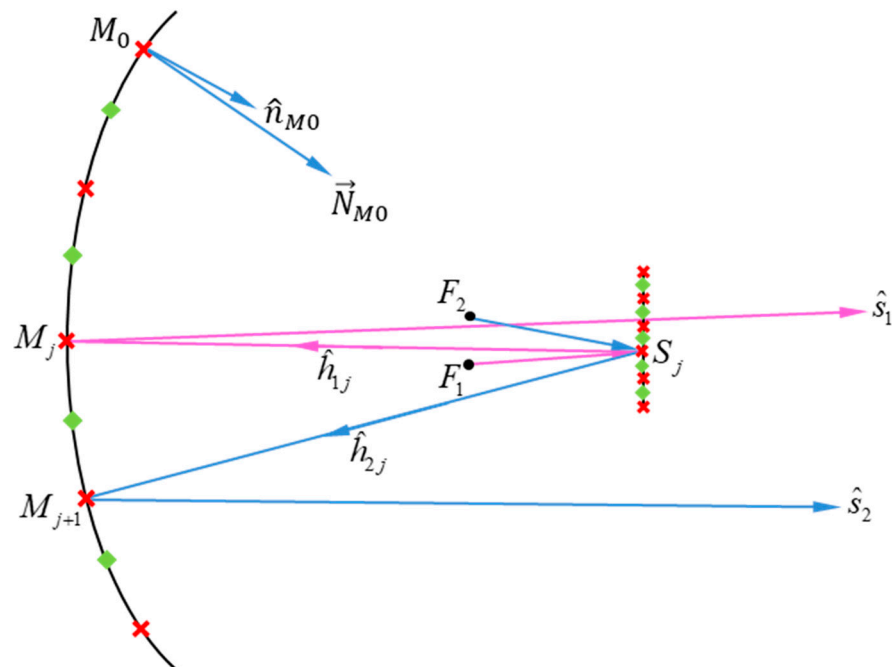


**Figure 3.** Bifocal reflectarray synthesis algorithm for a linear section. Two procedures were applied based on the same algorithm to double the density of data points: starting at a known point  $M_0$  on the main-RA to generate “x” points and starting at a known point  $S_0$  on the sub-RA to generating “♦” points. Both procedures lead to the same geometry.

The algorithm for bifocal synthesis illustrated in Figure 3 works as follows. Given a generic point  $M_j$  on the main-RA, along with its unit normal  $\hat{n}_{M_j}$  and the corresponding virtual normal  $\vec{N}_{M_j}$ , follow the next steps:

1. Extract the tangential part  $\vec{N}_{M_{\tau j}}$  of  $\vec{N}_{M_j}$  by (11):

$$\vec{N}_{M_{\tau j}} = \vec{N}_{M_j} - (\vec{N}_{M_j} \cdot \hat{n}_{M_j}) \hat{n}_{M_j}; \tag{13}$$

2. Compute the incident unit vector  $\hat{h}_{1j}$  at  $M_j$  by using (10):

$$\begin{aligned}\vec{s}_{1\tau} &= \hat{s}_1 - (\hat{s}_1 \cdot \hat{n}_{Mj}) \hat{n}_{Mj}, \quad \hat{h}_{1\tau j} = \vec{s}_{1\tau} - \vec{N}_{M\tau j}, \\ \hat{h}_{1j} &= \hat{h}_{1\tau j} - \hat{n}_{Mj} \sqrt{1 - |\hat{h}_{1\tau j}|^2};\end{aligned}\quad (14)$$

3. Determine the intersection point  $S_j$  between the incident ray  $\hat{h}_{1j}$  and the flat sub-RA, and obtain its unit normal  $\hat{n}_{Sj}$ .  
4. Calculate the incident ray at  $S_j$  as:

$$\hat{i}_{1j} = \frac{\overline{F_1 S_j}}{|\overline{F_2 S_j}|}; \quad (15)$$

5. Obtain the virtual normal at the sub-RA by using (5):

$$\vec{N}_{Sj} = \hat{h}_{1j} - \hat{i}_{1j}; \quad (16)$$

6. Extract the tangential part of  $\vec{N}_{Sj}$ :

$$\vec{N}_{S\tau j} = \vec{N}_{Sj} - \left( \vec{N}_{Sj} \cdot \hat{n}_{Sj} \right) \hat{n}_{Sj}; \quad (17)$$

7. Consider a focusing ray from  $\hat{s}_2$  to  $F_2$  through the point  $S_j$ . As the first step for this second ray, get the incident ray at sub-RA as:

$$\hat{i}_{2j} = \frac{\overline{F_2 S_j}}{|\overline{F_2 S_j}|}; \quad (18)$$

8. Calculate the reflected unit vector  $\hat{h}_{2j}$  at sub-RA by (9):

$$\begin{aligned}\vec{i}_{2\tau j} &= \hat{i}_{2j} - (\hat{i}_{2j} \cdot \hat{n}_{Sj}) \hat{n}_{Sj}, \quad \hat{h}_{2\tau j} = \vec{i}_{2\tau j} + \vec{N}_{S\tau j}, \\ \hat{h}_{2j} &= \hat{h}_{2\tau j} + \hat{n}_{Sj} \sqrt{1 - |\hat{h}_{2\tau j}|^2};\end{aligned}\quad (19)$$

9. Obtain the intersection point  $M_{j+1}$  between  $\hat{h}_{2j}$  and the main-RA and determine its unit normal  $\hat{n}_{M(j+1)}$ ;  
10. Get the virtual normal by using (5):

$$\vec{N}_{M(j+1)} = \hat{s}_2 - \hat{h}_{2j}; \quad (20)$$

11. Return to step 1 with point  $M_{j+1}$  and virtual normal  $\vec{N}_{M(j+1)}$ . The procedure is iterated several times until the main-RA is oversized.

Figure 3 illustrates this algorithm to obtain data points drawn with symbols “×”:

Another procedure can be established by starting at the sub-RA (known point  $S_0$  and known virtual normal  $\vec{N}_{S_0}$ ) by considering first steps 6 to 11 and then steps 1 to 5. The result will produce the set of data points drawn with symbols “◆” in Figure 3.

#### 4.2. 3D Extension with Two Foci

In the 3D extension of the bifocal synthesis algorithm, the steps described in Equations (13)–(20) remain valid with general vector relations. However, since the al-

gorithm generates data points along curved lines for both main-RA and sub-RA, it is necessary to use a set of starting points along central sections of both surfaces.

Figure 4 schematically illustrates how the algorithm evolves transversally from the central sections to produce the required set of data points across the aperture of the main-RA and sub-RA. In Figure 4 it has been assumed that the starting profile lies in the plane of symmetry, allowing the other half of the reflectarray surfaces to be defined by symmetry.

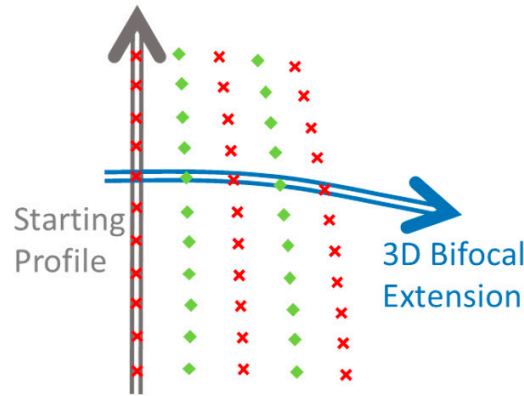


**Figure 4.** Bifocal reflectarray 3D synthesis scheme. A central section in the plane of symmetry is first synthesized as “Starting profile”. Then, starting at each point of the starting profile, a lateral strip is synthesized allowing the 3D extension of the reflectarray surface. Crosses are obtained by starting at the main-RA central section while diamonds are obtained by starting at sub-RA central section. The left part, not represented in the figure, is obtained by symmetry means.

#### 4.3. 3D Extension with Focal Ring

In the case of the 2D bifocal procedure applied starting at the vertex of a symmetric structure such as that of Figure 5, with two symmetric focal points ( $F_1, F_2$ ) and two focused scanned directions ( $\hat{s}_1, \hat{s}_2$ ), all of them contained in the plane XZ. The 3D extension of this central section by rotation about Z axis produces a symmetric dual configuration with a focal ring containing  $F_1$  and  $F_2$ . A feed located in a point of this focal ring would produce maximum radiation for a direction belonging to a focused cone containing  $\hat{s}_1$  and  $\hat{s}_2$ . Even if an offset section is selected, the same property remains. However, both the surface equations and the path length shift functions must be symmetric and will depend only on the radial coordinate  $\rho$ .

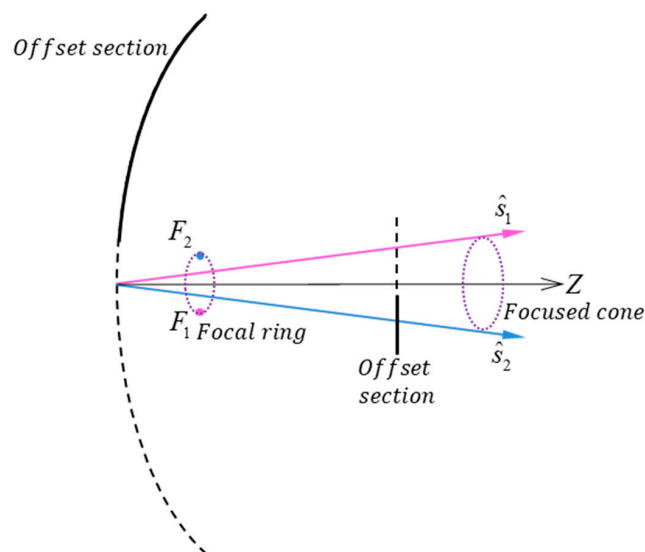


**Figure 5.** Bifocal 3D extension by rotation about the Z axis.

## 5. Numerical Results

Two different examples of dual bifocal reflectarray are presented. Both have been designed for a multi-beam onboard satellite antenna operating in the Ka band. The goal is to provide a high number of beams (around 100) with 0.65-degree beamwidth and a separation between contiguous beams of 0.56 degree, both in transmission and in the reception bands (in the 20 and 30 GHz bands, respectively). Adopting reflectarray surfaces, the number of antennas needed for full area coverage can be reduced from four to two. This is achieved by using the reflectarrays to provide two beams per feed by polarization discrimination. In this way, two of the four colors can be produced by a single multibeam antenna. More details of this application can be found in [5,6,9,11–14] showing different options based in single and dual reflectarray antennas.

In this paper, the details and simulated performance results of two bifocal reflectarray configurations are presented. Both configurations consist of a parabolic main-RA and flat sub-RA. A Cassegrain scheme with parabolic main reflector and hyperbolic subreflector is first defined as baseline design, as shown in Figure 6a. In the figure, the reference unit vectors of the feed system ( $\hat{x}_f, \hat{z}_f$ ) are depicted as well as those of the absolute system ( $\hat{x}, \hat{z}$ ). The unit vectors  $\hat{y}_f$  and  $\hat{y}$ , not represented, are normal to the plane of the figure. The main-RA will be supported by the same parabolic main reflector surface of the Cassegrain while two different options will be considered for the flat sub-RA. The first one is used to synthesize a bifocal configuration with a focal ring and a focused cone as shown in Figure 5. Since for this case the sub-RA surface must be symmetric about the Z axis, it must be normal to the Z axis (if a flat surface is required), otherwise it should be a curved surface. For instance, if a tilted section is chosen, the sub-RA would be a cone. The second option for the sub-RA is selected to synthesize a bifocal configuration with two focal points with the 3D extension shown in Figure 4. In this case, a tilted sub-RA plane is selected to be tangent to the hyperbolic surface at a central point adequately selected to reduce the average difference between the hyperbolic surface and the tangent plane. Both choices are depicted in Figure 6b.

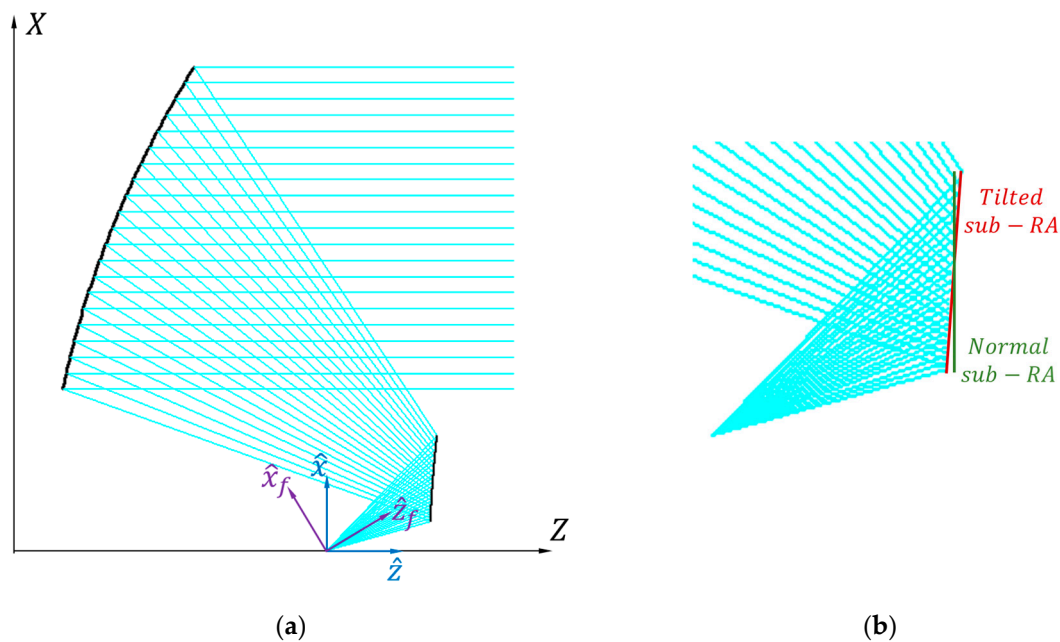


**Figure 6.** Baseline Cassegrain: (a) General view and ray tracing; (b) Detail of flat sub-RA.

The geometric parameters of the two baseline Cassegrain configurations are summarized in Table 1.

**Table 1.** Baseline Cassegrain Parameters.

Geometric Parameter	Symbol and Value
Main reflector aperture diameter	$D = 1.8$ m
Main reflector focal length	$f = 2.4$ m
Main reflector offset height	$h_{\text{off}} = 1.6$ m (focal ring design) $h_{\text{off}} = 1.8$ m (Two foci design)
Inter-focal length	$2c = 0.96$ m
Feed location	Feed = $(0, 0, -0.96)$ m
Magnification factor	$M = 1.25$

5.1. Focal Ring Bifocal Design

To achieve the desired scanning capability of the antenna, a focused cone with a central angle of  $1.68^\circ$  is enforced, along with a focal ring of radius 114 mm in the focal plane. This configuration ensures that the focused cone aligns with the map of beams, as shown in Figure 7, minimizing the mean scanning losses across the field of view. The map of beams depicted in Figure 7a shows two of the four colors which are necessary for the whole coverage by reusing two frequencies and two polarizations. Figure 7b shows schematically the cluster of feed apertures, each providing two beams. Two antennas would be necessary, each one providing two of the four colors. As can be seen in Figure 7b, the cluster of dual beams covers all the focal plane space, so a second antenna is necessary to provide the other two colors not represented in Figure 7a.

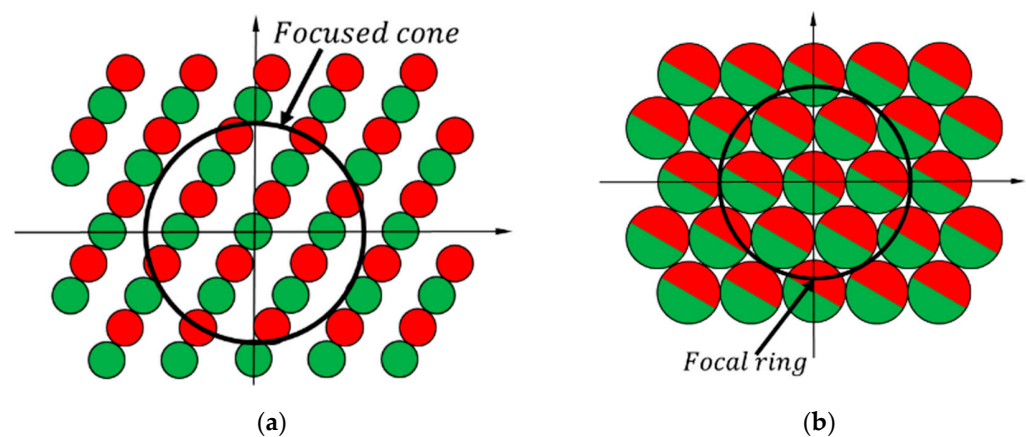


**Figure 7.** Multibeam configuration for one antenna (two are necessary for whole coverage): (a) map of beams, each color represents a different polarization; (b) feed cluster where each antenna generates two beams with perpendicular polarizations.

The sub-RA plane was selected to be normal to the Z axis (as shown in Figure 6b) and containing a central point of the original hyperbolic subreflector of the baseline Cassegrain configuration. The bifocal algorithm described in Section 4.1 was applied in the offset plane. The iterations of the algorithm started at the vertex of the parabola in the Z axis, generating a first set of data points. A second set of data points was obtained, as described in Section 4.1, starting from the vertex of the hyperbola in the Z axis. Due to the symmetry of the problem, only half of the data points (those corresponding to  $x \geq 0$ ) were used to adjust the polynomial approximation  $L(x)$ , according to Appendix B, but without considering  $z_y$ ,  $\partial L/\partial y$  or  $N_y$  since it is a 2D problem. The polynomial approximation was performed using the following basis functions:

$$L(x) = \sum_{n=0}^8 a_n \psi_n(x), \quad \frac{\partial L(x)}{\partial x} = \sum_{n=0}^8 a_n \psi'_n(x), \quad (21)$$

$$\psi_n(x) = x^n, \quad \psi'_n(x) = nx^{n-1}.$$

Figure 8 shows the derivative of  $L(x)$  as obtained from the bifocal synthesis algorithms through the computation of the virtual normal and the polynomial approximation used to characterize the reflectarrays. The maximum errors for these derivatives due to the polynomial approximation have been found to be less than  $5 \times 10^{-5}$  for the flat sub-RA and  $2 \times 10^{-5}$  for the parabolic main-RA. The global view of the path length shift  $L(x, y)$  is depicted in Figure 9. It must be taken into account that the function  $L$  is circularly symmetric, depending only on the radial cylindrical coordinate  $\rho$ .

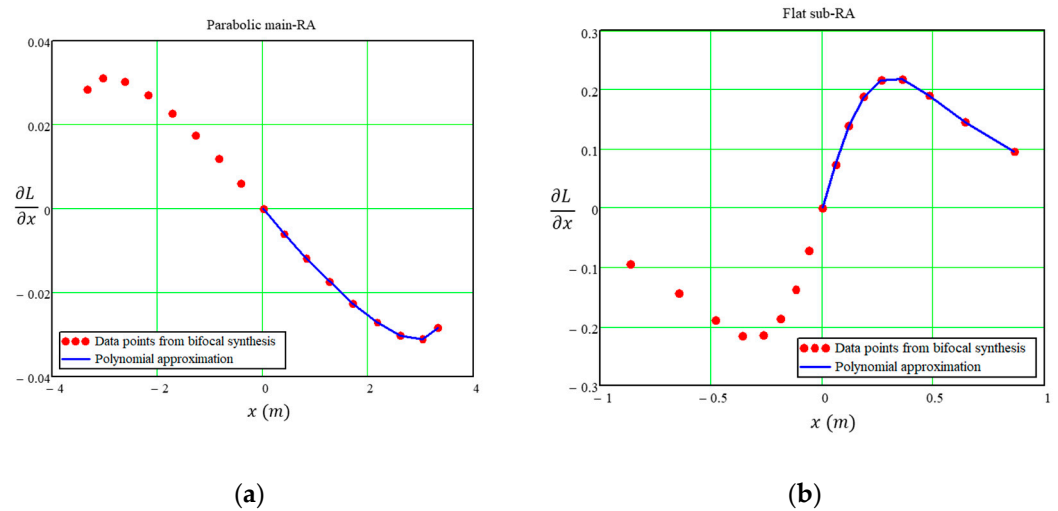


Figure 8. Derivatives of  $L(x)$  for the focal ring bifocal: (a) main-RA; (b) sub-RA.

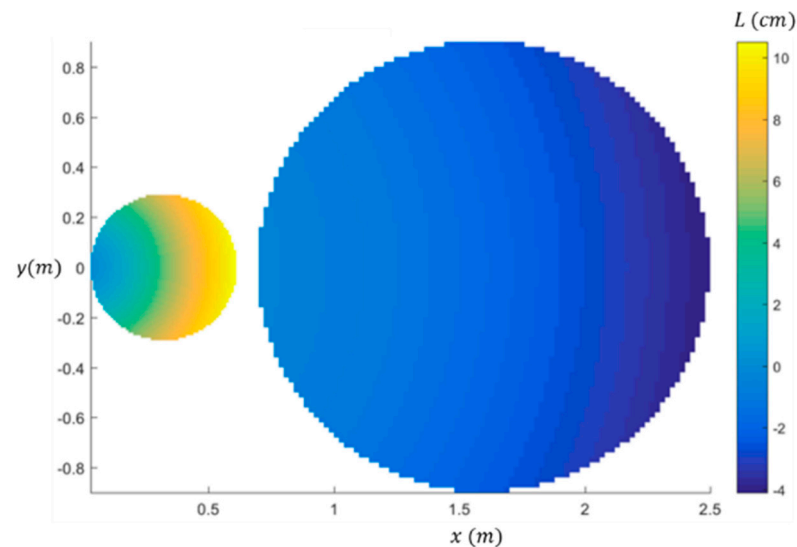


Figure 9. Path length shift distribution across the reflectarrays.

The focusing properties have been evaluated by GO and the results are depicted in Figure 10. A quasi-perfect focusing is achieved when scanning to  $\pm 1.68^\circ$  and the feed is located at the corresponding focal point. The case  $-1.68^\circ$  is quite good, but in general, scanning to negative values in the offset plane is worse than the corresponding positive value because the upper part of the subreflector, where the asymmetry due to the offset configuration is steeper, is used.

Basic Physical Optics (PO) simulations at 20 GHz have been developed by using in-house software tools [15,16] based on discretizing the surface in small triangular patches. The implementation of the impact of the phase shift due to the reflectarrays has been performed by multiplying the currents predicted using PO by the phase shift term (propor-

tional to the path length) computed at the center of each patch. Ideal feed models of cos-q type have been adopted, providing edge taper illumination of  $-12$  dB. Figure 11 shows the PO patterns for the bifocal design with focal ring when the feed is located to make the antenna scan in the boresight direction and in the  $\theta = 1.68^\circ$  for the principal cuts. The scanning behavior of the antenna is satisfactory. The lack of symmetry observed in the XZ plane is a result of the offset configuration employed in the design.

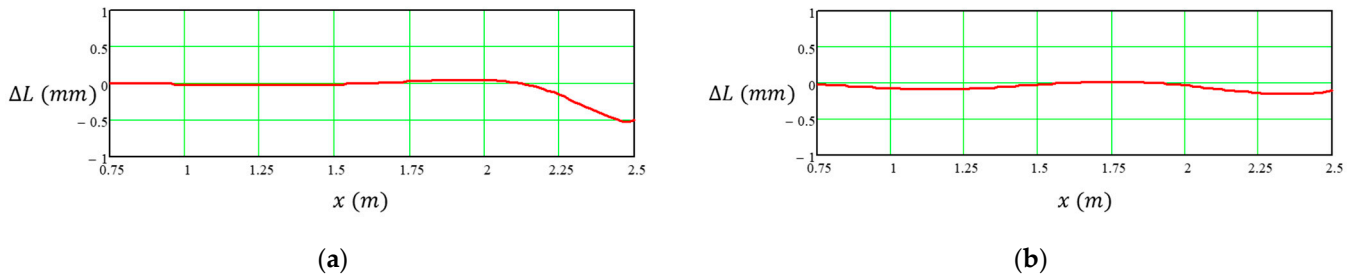


Figure 10. Ripple of the path length shift ( $\Delta L$ ) across the main-RA aperture when scanning: (a) to  $-1.68^\circ$ ; (b) to  $+1.68^\circ$ .

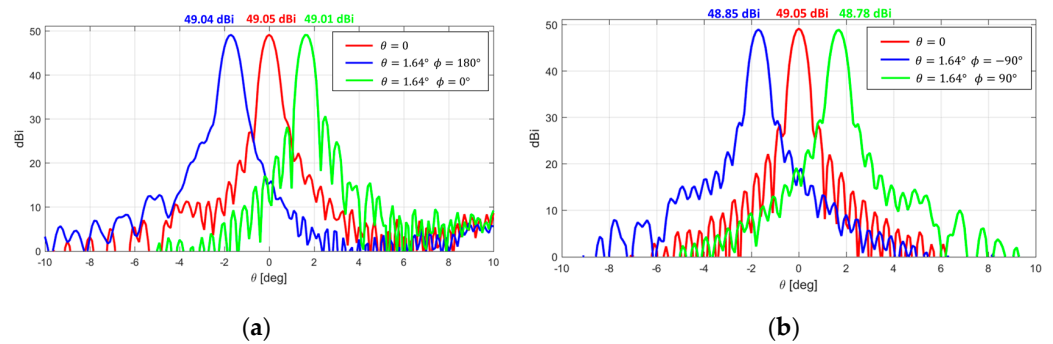
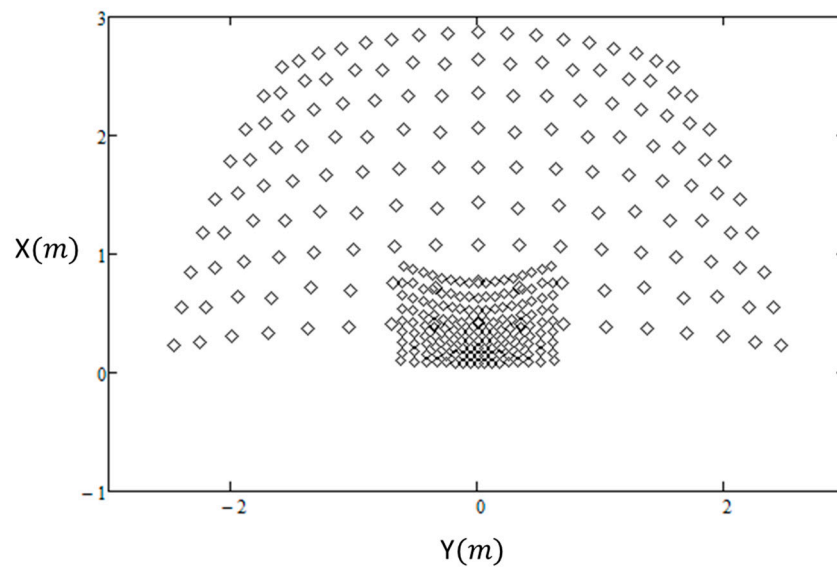


Figure 11. PO patterns at 20 GHz: (a) XZ cut; (b) YZ cut.

### 5.2. Bifocal Design with Two Focal Points

In this design, two focal points were selected to correspond to scanning directions at  $\theta = 1.68^\circ$  in the YZ plane ( $\phi = 90^\circ$  and  $\phi = -90^\circ$ ). The focal points were chosen to replicate the same deviation factor as in the baseline Cassegrain design in order to maintain the size of the sub-RA. In this design, the sub-RA plane is the tilted version of Figure 6b, and a feed plane normal to the  $\hat{z}_f$  direction was considered. The  $\hat{z}_f$  direction points from the original feed point in the baseline Cassegrain to the bisector direction of the sub-RA. The two focal points were chosen in this feed plane by GO calculations in the baseline Cassegrain. Two sets of rays incoming to the main reflector from the focal directions ( $\theta = 1.68^\circ, \phi = \pm 90^\circ$ ) are considered. After reflection of the sets of rays at main reflector and subreflector, the best focusing points at the feed plane are computed, providing the coordinates of the focal points at  $(0, -0.0952, -0.96)$  for  $\phi = 90^\circ$  and  $(0, 0.0952, -0.96)$  for  $\phi = -90^\circ$ .

Before synthesizing the 3D main-RA and sub-RA as described in Section 4.2, a central section of the reflectarrays is synthesized in the offset ZX plane. A bifocal central section is initially synthesized with focal directions ( $\theta = 1.68^\circ, \phi = 0^\circ$  and  $180^\circ$ ). In this case, the focal points are also taken in the feed plane at the coordinates  $(-0.084929, 0, -0.911868)$  for  $\phi = 0^\circ$  and  $(0.081149, 0, -1.00599)$  for  $\phi = 180^\circ$ . The set of data points from the central section is then used to extend the synthesis in 3D, resulting a set of data points as depicted in Figure 12.



**Figure 12.** Set of data points obtained for the synthesis of the bifocal dual reflectarray.

With the synthesized sets of data for the derivatives of the path length shift for main-RA and sub-RA, a polynomial interpolation was constructed by using the following basi functions:

$$L(x, y) = \sum_{j=0}^2 \sum_{i=0}^3 p_{ij} \psi_{ij}(x, y), \quad \psi_{ij}(x, y) = x^i y^{2j+1} \tag{22}$$

The data points used for interpolation exceed the area of the main-RA and sub-RA. This is convenient to improve the accuracy of the polynomial approximations. The view of the path length shift distribution and those of the phase delay distributions for both reflectarrays are plotted in Figure 13. It can be observed that a deeper variation in path length shift variation is required for the flat sub-RA than for the main reflector. The error due to the polynomial interpolation for the partial derivatives has been found to be less than  $5 \times 10^{-3}$  for the flat sub-RA and less than  $2 \times 10^{-3}$  for the main-RA.

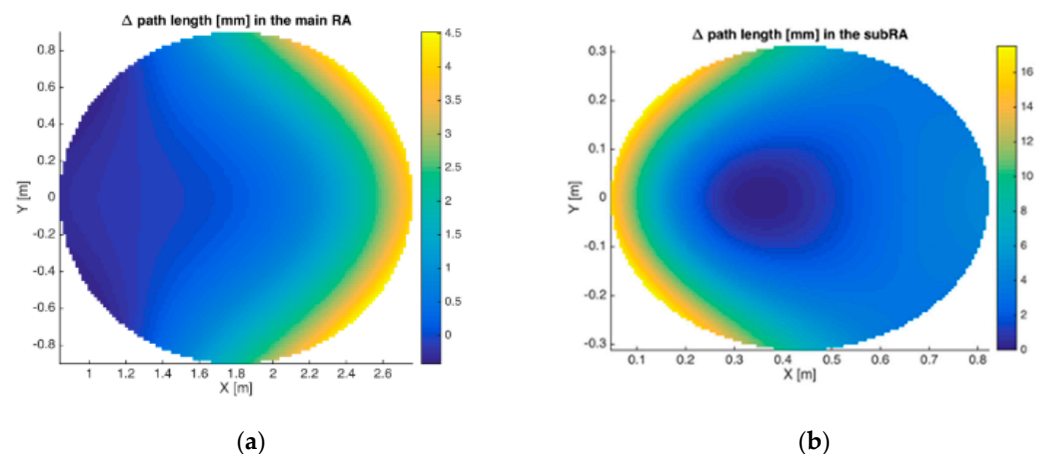


**Figure 13.** Path length shift of the bifocal dual reflectarray with two focal points: (a) main-RA; (b) sub-RA.

To verify the focusing properties of the designed bifocal dual reflectarray, the uniformity of the phase distribution across the scanned aperture was studied by analyzing the root mean square (rms) of the path length after GO simulations. Figure 14 compares the path length rms when the antenna scans in the plane of the foci compared to that of the baseline Cassegrain.

Again, basic Physical Optics (PO) simulations at 20 GHz were performed using the same approximations adopted in Section 5.1. Figure 15 show the Physical Optics patterns for the bifocal design with two foci when the antenna scans in the plane where the focusing directions are located. The maximum ripple of the gain for the considered beams, extending beyond the focal directions is approximately 0.2 dB compared to about 0.5 dB ripple observed in the baseline Cassegrain configuration.

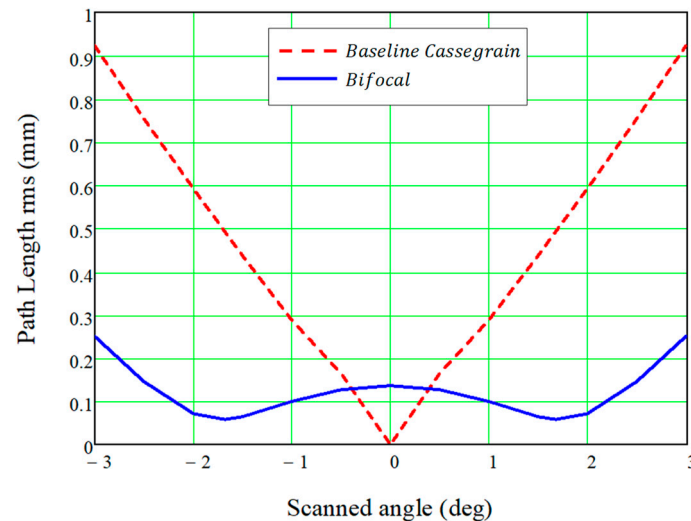


**Figure 14.** Path length rms of the scanned aperture for the bifocal and the Cassegrain.

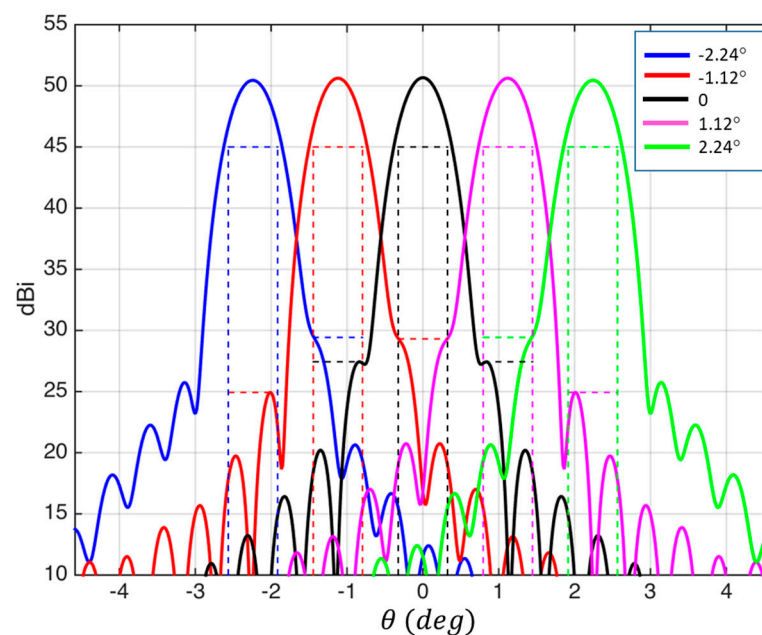


**Figure 15.** Physical Optics patterns for the bifocal design with two foci. Dotted lines depict masks of requirements for main lobe and side lobes.

## 6. Conclusions

In this paper, a novel vector formulation has been proposed for the synthesis of curved reflectarrays using ray tracing techniques. The concept of path length shift, which is directly proportional to the phase distribution, has been introduced and applied to solve the first stage of the reflectarray synthesis problem without restrictions in frequency. The concept of virtual normal, which characterizes the reflection law at the reflectarray surface, enables the vector formulation of ray tracing for curved reflectarrays. Equations have been developed

to establish the relationship between the virtual normal, obtained in the GO synthesis, and the derivatives of the path length shift distribution with respect to the coordinates of the aperture of the curved reflectarray. The path length shift, and, hence, the phase distribution is then reconstructed by an interpolation scheme that is also presented. This interpolation minimizes, in a least mean squares sense, the differences between the synthesized derivatives of the path length shift, as obtained from the GO synthesis, and the derivatives of the interpolation polynomial.

Two different configurations of bifocal dual reflectarrays have been presented, along with numerical results that demonstrate the feasibility of the proposed solution. In the first configuration, a focal ring is generated in the focal plane, improving the antenna's field of view when a cluster of feeds is used to achieve a multibeam antenna, as opposed to the standard case of having a single focal point. The reflectarray synthesis in this configuration is a 2D problem, and the 3D extension is obtained through the rotational symmetry of the phase shift synthesized using the bifocal technique in the central section of the surfaces. In the second configuration, a 3D synthesis problem is solved to produce two foci in the horizontal plane of the antenna, resulting in enhanced scanning performance in such plane.

**Author Contributions:** Conceptualization, A.P., O.R., J.A.E. and G.T.; methodology, A.P., E.M.-d.-R., D.M.-d.-R., M.A. and J.A.E.; software, A.P., Y.R.-V., E.M.-d.-R., D.M.-d.-R., B.G.-V. and M.A.; writing—original draft preparation, A.P. and Y.R.-V.; writing—review and editing, J.A.E., M.A., E.M.-d.-R. and G.T.; supervision, G.T.; project administration, A.P., J.A.E. and G.T. All authors have read and agreed to the published version of the manuscript.

**Funding:** This research was funded in part by the Spanish Ministry of Economy and Competitiveness under Project PDC2021-120959-C21/C22, in part by the Spanish Ministry of Science and Innovation MCIN/AEI/10.13039/501100011033 under project RYC2021-033593-I and by the European Union NextGeneration EU/PRTR, in part by the Regional Government of Galicia under projects GRC-ED431C-2019/25 and agreement for funding AtlantTIC, and in part by the European Space Agency ESTEC under Contract 4000117113/16/NL/AF.

**Data Availability Statement:** The data presented in this study are available on request from the corresponding author. The data are not publicly available due to privacy concerns.

**Conflicts of Interest:** The authors declare no conflict of interest.

## Appendix A. Computation of the Tangential Part of the Virtual Normal

Let  $\vec{r}(x, y)$  be the location of any point of the surface. The surface and its partial derivatives can be expressed as:

$$\begin{aligned}\vec{r}(x, y) &= x\hat{x} + y\hat{y} + z(x, y)\hat{z}, \\ \vec{r}_x(x, y) &= \hat{x} + z_x(x, y)\hat{z}, \quad \vec{r}_y(x, y) = \hat{y} + z_y(x, y)\hat{z}.\end{aligned}\tag{A1}$$

Then, the unit normal vector can be written as:

$$\hat{n} = \frac{\vec{r}_x \times \vec{r}_y}{|\vec{r}_x \times \vec{r}_y|} = \frac{-z_x\hat{x} - z_y\hat{y} + \hat{z}}{\sqrt{1 + z_x^2 + z_y^2}}\tag{A2}$$

A local system  $\{\hat{u}, \hat{v}, \hat{n}\}$  can be defined at each reflection point  $R$  so that  $\hat{u} = \vec{r}_x / |\vec{r}_x|$  and  $\hat{v} = \vec{r}_y / |\vec{r}_y|$  are tangent to the surface and  $\hat{n}$  is normal to it. The following matrix

formulation can be written for the transformation from the Cartesian system to the local system  $\{\hat{u}, \hat{v}, \hat{n}\}$ :

$$\begin{bmatrix} \hat{u} \\ \hat{v} \\ \hat{n} \end{bmatrix} = \begin{bmatrix} \frac{1}{C_x} & 0 & \frac{z_x}{C_x} \\ 0 & \frac{1}{C_y} & \frac{z_y}{C_y} \\ \frac{-z_x}{C} & \frac{-z_y}{C} & \frac{1}{C} \end{bmatrix} \begin{bmatrix} \hat{x} \\ \hat{y} \\ \hat{z} \end{bmatrix}, \tag{A3}$$

$$C_x = \sqrt{1 + z_x^2}, C_y = \sqrt{1 + z_y^2}, C = \sqrt{1 + z_x^2 + z_y^2}.$$

Although  $\hat{u}$  and  $\hat{v}$  are not perpendicular to each other, the election is interesting because each of them is contained in the respective plane XZ or YZ. The tangential coordinates along  $\hat{u}$  and  $\hat{v}$  can be projected on the axis X and Y, giving the following simple relations:

$$\begin{bmatrix} \frac{\partial u}{\partial x} & \frac{\partial v}{\partial x} \\ \frac{\partial u}{\partial y} & \frac{\partial v}{\partial y} \end{bmatrix} = \begin{bmatrix} C_x & 0 \\ 0 & C_y \end{bmatrix}. \tag{A4}$$

Consequently:

$$\begin{bmatrix} \frac{\partial L}{\partial x} \\ \frac{\partial L}{\partial y} \end{bmatrix} = \begin{bmatrix} \frac{\partial u}{\partial x} & \frac{\partial v}{\partial x} \\ \frac{\partial u}{\partial y} & \frac{\partial v}{\partial y} \end{bmatrix} \begin{bmatrix} \frac{\partial L}{\partial u} \\ \frac{\partial L}{\partial v} \end{bmatrix} = \begin{bmatrix} C_x & 0 \\ 0 & C_y \end{bmatrix} \begin{bmatrix} \frac{\partial L}{\partial u} \\ \frac{\partial L}{\partial v} \end{bmatrix}. \tag{A5}$$

Consider now an orthonormal system  $(\hat{\alpha}, \hat{\beta}, \hat{n})$  so that  $\hat{\alpha}$  is in the direction of  $\vec{N}_T$  while  $\hat{\beta}$  is perpendicular. The following transformation matrix can be established, according to Figure A1:

$$\begin{bmatrix} \hat{u} \\ \hat{v} \end{bmatrix} = \begin{bmatrix} \cos(\delta) & \sin(\delta) \\ \cos(\delta + \gamma) & \sin(\delta + \gamma) \end{bmatrix} \begin{bmatrix} \hat{\alpha} \\ \hat{\beta} \end{bmatrix} = \begin{bmatrix} \hat{u} \cdot \hat{\alpha} & \hat{u} \cdot \hat{\beta} \\ \hat{v} \cdot \hat{\alpha} & \hat{v} \cdot \hat{\beta} \end{bmatrix} \begin{bmatrix} \hat{\alpha} \\ \hat{\beta} \end{bmatrix}. \tag{A6}$$

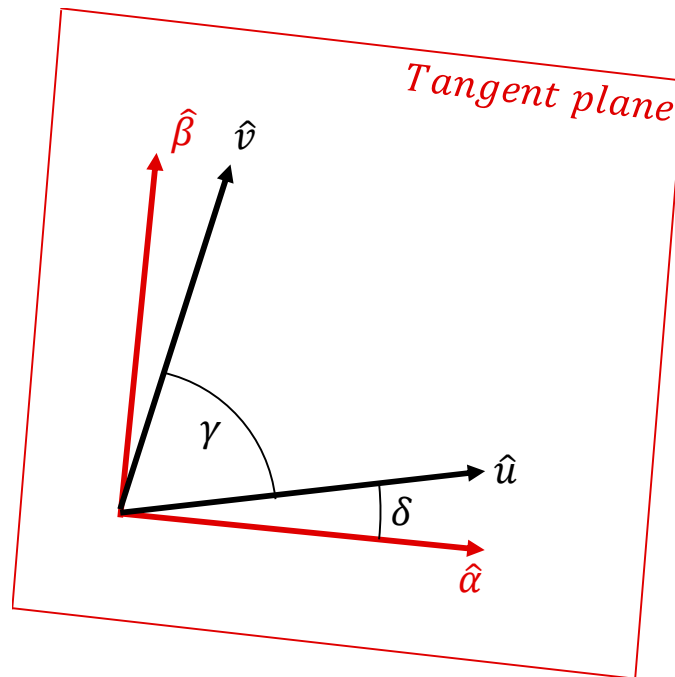


Figure A1. Transformation of the vectors  $(\hat{u}, \hat{v})$  to obtain the orthonormal system  $(\hat{\alpha}, \hat{\beta})$ .

The mapping transformation between the coordinates  $(u, v)$  and  $(\alpha, \beta)$  can be written with the transposed matrix as:

$$\begin{bmatrix} \alpha \\ \beta \end{bmatrix} = \begin{bmatrix} \cos(\delta) & \cos(\delta + \gamma) \\ \sin(\delta) & \sin(\delta + \gamma) \end{bmatrix} \begin{bmatrix} u \\ v \end{bmatrix} = \begin{bmatrix} \hat{u} \cdot \hat{\alpha} & \hat{v} \cdot \hat{\alpha} \\ \hat{u} \cdot \hat{\beta} & \hat{v} \cdot \hat{\beta} \end{bmatrix} \begin{bmatrix} u \\ v \end{bmatrix}. \tag{A7}$$

The derivatives  $\partial L / \partial u$  and  $\partial L / \partial v$  can be expressed as:

$$\begin{bmatrix} \frac{\partial L}{\partial u} \\ \frac{\partial L}{\partial v} \end{bmatrix} = \begin{bmatrix} \frac{\partial \alpha}{\partial u} & \frac{\partial \beta}{\partial u} \\ \frac{\partial \alpha}{\partial v} & \frac{\partial \beta}{\partial v} \end{bmatrix} \begin{bmatrix} \frac{\partial L}{\partial \alpha} \\ \frac{\partial L}{\partial \beta} \end{bmatrix} = \begin{bmatrix} \hat{u} \cdot \hat{\alpha} & \hat{u} \cdot \hat{\beta} \\ \hat{v} \cdot \hat{\alpha} & \hat{v} \cdot \hat{\beta} \end{bmatrix} \begin{bmatrix} \frac{\partial L}{\partial \alpha} \\ \frac{\partial L}{\partial \beta} \end{bmatrix}. \tag{A8}$$

Since  $\hat{\alpha}$  has been chosen along  $\vec{N}_\tau$ , the following simplifications hold:

$$\vec{N}_\tau = \frac{\partial L}{\partial \alpha} \hat{\alpha}, \frac{\partial L}{\partial \beta} = 0 \implies \begin{bmatrix} \frac{\partial L}{\partial u} \\ \frac{\partial L}{\partial v} \end{bmatrix} = \begin{bmatrix} \hat{u} \cdot \hat{\alpha} \\ \hat{v} \cdot \hat{\alpha} \end{bmatrix} \frac{\partial L}{\partial \alpha} = \begin{bmatrix} \hat{u} \cdot \vec{N}_\tau \\ \hat{v} \cdot \vec{N}_\tau \end{bmatrix}. \tag{A9}$$

Combining (A5) and (A9), enables to write:

$$\begin{bmatrix} \frac{\partial L}{\partial x} \\ \frac{\partial L}{\partial y} \end{bmatrix} = \begin{bmatrix} C_x & 0 \\ 0 & C_y \end{bmatrix} = \begin{bmatrix} C_x & 0 \\ 0 & C_y \end{bmatrix} \begin{bmatrix} \frac{1}{C_x} & 0 \\ 0 & \frac{1}{C_y} \end{bmatrix} \begin{bmatrix} \frac{z_x}{C_x} \\ \frac{z_y}{C_y} \end{bmatrix} \begin{bmatrix} N_x \\ N_y \\ N_z \end{bmatrix}, \tag{A10}$$

which can be simplified as:

$$\begin{bmatrix} \frac{\partial L}{\partial x} \\ \frac{\partial L}{\partial y} \end{bmatrix} = \begin{bmatrix} 1 & 0 & z_x \\ 0 & 1 & z_y \end{bmatrix} \begin{bmatrix} N_x \\ N_y \\ N_z \end{bmatrix}. \tag{A11}$$

Taking into consideration that  $\vec{N}_\tau$  has no normal component, its Cartesian components are not independent, and the following condition must be satisfied:

$$\vec{N}_\tau \cdot \hat{n} = 0 \implies N_z = z_x N_x + z_y N_y. \tag{A12}$$

The expression (A11) can be written in terms of only  $N_x$  and  $N_y$  by introducing the condition (A12):

$$\begin{bmatrix} \frac{\partial L}{\partial x} \\ \frac{\partial L}{\partial y} \end{bmatrix} = \begin{bmatrix} 1 + z_x^2 & z_x z_y \\ z_x z_y & 1 + z_y^2 \end{bmatrix} \begin{bmatrix} N_x \\ N_y \end{bmatrix}. \tag{A13}$$

An inverse expression can be obtained directly as:

$$\begin{bmatrix} N_x \\ N_y \end{bmatrix} = \frac{1}{1 + z_x^2 + z_y^2} \begin{bmatrix} 1 + z_y^2 & -z_x z_y \\ -z_x z_y & 1 + z_x^2 \end{bmatrix} \begin{bmatrix} \frac{\partial L}{\partial x} \\ \frac{\partial L}{\partial y} \end{bmatrix}. \tag{A14}$$

Finally, (A14) can be completed with the  $N_z$  component, as expressed in (A12), giving the following relation:

$$\begin{bmatrix} N_x \\ N_y \\ N_z \end{bmatrix} = \frac{1}{1 + z_x^2 + z_y^2} \begin{bmatrix} 1 + z_y^2 & -z_x z_y \\ -z_x z_y & 1 + z_x^2 \\ z_x & z_y \end{bmatrix} \begin{bmatrix} \frac{\partial L}{\partial x} \\ \frac{\partial L}{\partial y} \end{bmatrix}. \tag{A15}$$

### Appendix B. Least Squares Interpolation to Compute the Path Length Shift

Let  $L(x, y)$  be a function with known values  $L_k$  at a set of data points  $(x_k, y_k)$ . It is possible to estimate the function  $L(x, y)$  by a series expansion using known basis func-

tions  $\psi_n(x, y)$ . Usually polynomial functions are selected, but the formulation is described here in general. The series expansion is written as:

$$L(x, y) = \sum_n a_n \psi_n(x, y), \tag{A16}$$

where  $a_n$  are coefficients to be determined. The least squares condition is based on minimizing the following error function:

$$\varepsilon(\bar{a}) = \sum_k \left( \sum_n a_n \psi_n(x_k, y_k) - L_k \right)^2. \tag{A17}$$

To achieve such minimization, the derivatives of  $\varepsilon(\bar{a})$  respect to every unknown term  $a_m$  are neglected:

$$\frac{\partial \varepsilon(\bar{a})}{\partial a_m} = \sum_k 2 \left( \sum_n a_n \psi_n(x_k, y_k) - L_k \right) \psi_m(x_k, y_k) = 0. \tag{A18}$$

Last expression can be rewritten by denoting  $\psi_n^k = \psi_n(x_k, y_k)$  :

$$\sum_n a_n \left( \sum_k \psi_n^k \psi_m^k \right) = \sum_k L_k \psi_m^k. \tag{A19}$$

For each basis function (numbered by  $m$ ), it is possible to write an equation such as (A19). The set of equations admits a matrix formulation as the following example (for three basis functions):

$$\begin{bmatrix} \sum_k \psi_1^k \psi_1^k & \sum_k \psi_1^k \psi_2^k & \sum_k \psi_1^k \psi_3^k \\ \sum_k \psi_2^k \psi_1^k & \sum_k \psi_2^k \psi_2^k & \sum_k \psi_2^k \psi_3^k \\ \sum_k \psi_3^k \psi_1^k & \sum_k \psi_3^k \psi_2^k & \sum_k \psi_3^k \psi_3^k \end{bmatrix} \begin{bmatrix} a_1 \\ a_2 \\ a_3 \end{bmatrix} = \begin{bmatrix} \sum_k \psi_1^k L_k \\ \sum_k \psi_2^k L_k \\ \sum_k \psi_3^k L_k \end{bmatrix}. \tag{A20}$$

This can be generalized for any number of basis functions with the following matrix formulation:

$$[\Psi \Psi^T] [A] = [\Psi L], \Psi_{n,k} = \psi_n^k, A_n = a_n, L_k = L_k. \tag{A21}$$

The unknown vector of coefficients  $\{a_n\}$  to develop the interpolation (A16) is then determined as:

$$[A] = [\Psi \Psi^T]^{-1} [\Psi L]. \tag{A22}$$

Although the size of the matrix  $\Psi$  is  $N \times K$ , being  $N$  the number of basis functions and  $K$  the number of data points across the reflectarray, the matrix  $\Psi \Psi^T$ , which must be inverted in (A22), is only  $N \times N$ .

If the partial derivatives  $L_{xk}, L_{yk}$  are known at a set of points rather than the function itself, the interpolation formula (A16) can be adopted, but an alternative least squares error function is adopted for the minimization:

$$\delta(\bar{a}) = \sum_k \left( \sum_n a_n \psi_{xn}(x_k, y_k) - L_{xk} \right)^2 + \left( \sum_n a_n \psi_{yn}(x_k, y_k) - L_{yk} \right)^2, \tag{A23}$$

where  $\psi_{xn}$  and  $\psi_{yn}$  are the derivatives of the basis function  $\psi_n$  respect to  $x$  and  $y$ , respectively. A similar formulation can be developed by denoting the derivatives of the basis functions at the data points by  $\psi_{xn}^k = \psi_{xn}(x_k, y_k)$ ,  $\psi_{yn}^k = \psi_{yn}(x_k, y_k)$ :

$$\frac{\partial \delta(\bar{a})}{\partial a_m} = \sum_k \left\{ 2 \left( \sum_n a_n \psi_{xn}^k - L_{xk} \right) \psi_{xm}^k + 2 \left( \sum_n a_n \psi_{yn}^k - L_{yk} \right) \psi_{ym}^k \right\} = 0, \quad (\text{A24})$$

which can be rewritten as:

$$\sum_n a_n \left( \sum_k \psi_{xn}^k \psi_{xm}^k + \psi_{yn}^k \psi_{ym}^k \right) = \sum_k L_{xk} \psi_{xm}^k + L_{yk} \psi_{ym}^k, \quad (\text{A25})$$

Again, a matrix formulation is possible:

$$\begin{aligned} [\Psi_X \Psi_X^T + \Psi_Y \Psi_Y^T] [A] &= [\Psi_X L_X + \Psi_Y L_Y], \\ \Psi_{Xn,k} &= \psi_{xn}^k, \quad \Psi_{Yn,k} = \psi_{yn}^k, \\ A_n &= a_n, \quad L_{Xk} = L_{xk}, \quad L_{Yk} = L_{yk} \end{aligned} \quad (\text{A26})$$

The unknown vector of coefficients is then obtained as:

$$[A] = [\Psi_X \Psi_X^T + \Psi_Y \Psi_Y^T]^{-1} [\Psi_X L_X + \Psi_Y L_Y] \quad (\text{A27})$$

## References

- Schneider, M.; Hartwanger, C.; Wolf, H. Antennas for multiple spot beams satellites. *CEAS Space J.* **2011**, *2*, 59–66. [\[CrossRef\]](#)
- Rao, B.L. Bifocal dual reflector antenna. *IEEE Trans. Antennas Propag.* **1974**, *22*, 711–714. [\[CrossRef\]](#)
- Rappaport, C. An offset bifocal reflector antenna design for wide-angle beam scanning. *IEEE Trans. Antennas Propag.* **1984**, *32*, 1196–1204. [\[CrossRef\]](#)
- Pino, A.G.; Llombart, N.; González-Valdés, B.; Rubiños, O. A Bifocal Ellipsoidal Gregorian Reflector System for THz Imaging Applications. *IEEE Trans. Antennas Propag.* **2012**, *60*, 4119–4129. [\[CrossRef\]](#)
- Martínez-de-Rioja, E.; Martínez-de-Rioja, D.; Encinar, J.A.; Pino, A.; Gonzalez-Valdes, B.; Rodriguez-Vaqueiro, Y.; Arias, M.; Toso, G. Advanced Multibeam Antenna Configurations Based on Reflectarrays: Providing Multispot Coverage with a Smaller Number of Apertures for Satellite Communications in the K and Ka Bands. *IEEE Antennas Propag. Mag.* **2019**, *61*, 77–86. [\[CrossRef\]](#)
- Martínez-de-Rioja, E.; Encinar, J.A.; Pino, A.; Rodriguez-Vaqueiro, Y. Broadband Linear-to-Circular Polarizing Reflector for Space Applications in Ka-Band. *IEEE Trans. Antennas Propag.* **2020**, *68*, 6826–6831. [\[CrossRef\]](#)
- Menzel, W.; Al-Tikriti, M.; Leberer, R. A 76 GHz multiple-beam planar reflector antenna. In Proceedings of the 32nd European Microwave Conference, Milan, Italy, 23–26 September 2002. [\[CrossRef\]](#)
- Cuevas, J.G.; Tienda, C.; Encinar, J.A.; Krieger, G. Principle of bifocal antennas implemented in a dual reflectarray configuration. In Proceedings of the 9th European Conference on Antennas and Propagation (EUCAP), Lisbon, Portugal, 12–17 April 2015.
- Martínez-de-Rioja, E.; Encinar, J.A.; Pino, A.; González-Valdés, B.; Hum, S.V.; Tienda, C. Bifocal Design Procedure for Dual-Reflectarray Antennas in Offset Configurations. *IEEE Antennas Wirel. Propag. Lett.* **2018**, *17*, 1421–1425. [\[CrossRef\]](#)
- Leberer, R.; Menzel, W. A dual planar reflectarray with synthesized phase and amplitude distribution. *IEEE Trans. Antennas Propag.* **2005**, *53*, 3534–3539. [\[CrossRef\]](#)
- Pino, A.; Rodríguez-Vaqueiro, Y.; González-Valdés, B.; Rubiños, O.; Martínez-de-Rioja, E.; Encinar, J.A.; Toso, G. Design of a Bifocal dual Reflectarray System with Parabolic Main Surface for a Multifed Space Antenna. In Proceedings of the IEEE International Symposium on Antennas and Propagation and USNC-URSI Radio Science Meeting (APS/URSI), Boston, MA, USA, 8–13 July 2018. [\[CrossRef\]](#)
- Martínez-de-Rioja, D.; Martínez-de-Rioja, E.; Rodríguez-Vaqueiro, Y.; Encinar, J.A.; Pino, A. Multibeam Reflectarrays in Ka-Band for Efficient Antenna Farms Onboard Broadband Communication Satellites. *Sensors* **2021**, *21*, 207. [\[CrossRef\]](#) [\[PubMed\]](#)
- Martínez-de-Rioja, E.; Encinar, J.A.; Toso, G. Bifocal Dual-Reflectarray Antenna to Generate a Complete Multiple Spot Beam Coverage for Satellite Communications in Ka-Band. *Electronics* **2020**, *9*, 961. [\[CrossRef\]](#)
- Martínez-de-Rioja, D.; Martínez-de-Rioja, E.; Rodríguez-Vaqueiro, Y.; Encinar, J.A.; Pino, A.; Arias, M.; Toso, G. Transmit–Receive Parabolic Reflectarray to Generate Two Beams per Feed for Multispot Satellite Antennas in Ka-Band. *IEEE Trans. Antennas Propag.* **2021**, *69*, 2673–2685. [\[CrossRef\]](#)

15. Martínez, J.A.; Pino, A.G.; Vega, I.; Arias, M.; Rubiños, O. ICARA: Induced current analysis of reflector antennas. *IEEE Antennas Propag. Mag.* **2005**, *47*, 92–100. [[CrossRef](#)]
16. Arias-Acuña, M.; García-Pino, A.; Rubiños-López, O. Fast Far Field Computation of Single and Dual Reflector Antennas. *J. Eng.* **2013**, *2013*, 140254. [[CrossRef](#)]

**Disclaimer/Publisher's Note:** The statements, opinions and data contained in all publications are solely those of the individual author(s) and contributor(s) and not of MDPI and/or the editor(s). MDPI and/or the editor(s) disclaim responsibility for any injury to people or property resulting from any ideas, methods, instructions or products referred to in the content.